Supplementary Information:
Ion imaging of spatially inhomogeneous nanoplasmas in NaCl particles

Loren Ban, Hanchao Tang[a], Jonas Heitland[a], Christopher W. West, Bruce L. Yoder, Ioannis Thanopulos, Ruth Signorell

1. Experimental details

Particle size distribution was monitored and measured concurrently to the photoemission experiment with a scanning mobility particle sizer (SMPS) device. An example of the size distribution of NaCl particles is shown in Figure S1. The particles generated by the atomizer have a mean diameter of 124 nm, with a geometric standard deviation of 1.7. The maximum is observed at 102 nm.
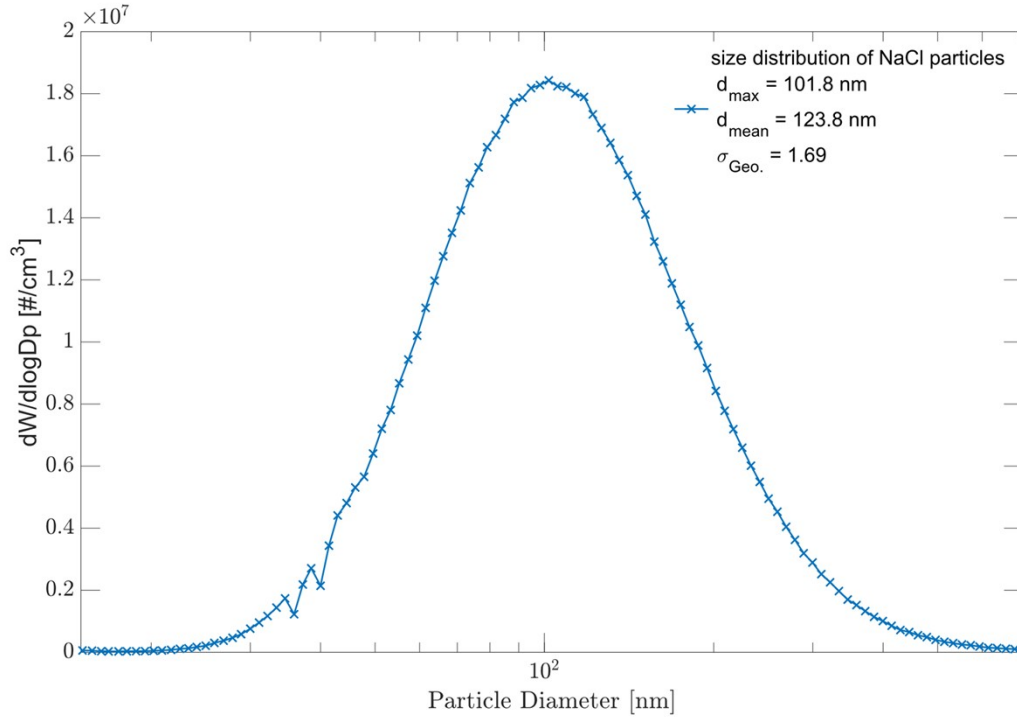
Figure S1 Particle size distribution of NaCl particles measured with the SMPS. Mean particle diameter is 124 nm with a geometric standard deviation of 1.7.

To calibrate the peak Intensity of NIR pulses with above threshold ionization (ATI) the following equation was employed.

$$eKE = nh\nu - I_p - U_p$$

eKE means kinetic energy of electrons, which can be measured directly. *n*, *h* and *v* correspond to the number of photons used for ionization, the Planck constant and the frequency of the incident light, respectively. I_p is the ionization potential of the substance and U_p represents the pondermotive energy resulting from the strong laser field applied to the substance. U_p depends on light intensity *I* and is given by

$$U_p = \frac{2e^2}{c\epsilon_0 m} \cdot \frac{I}{4\omega_0^2}$$

where e is the electron charge, c is the speed of light, ϵ_0 is the vacuum permittivity, m is the electron mass, and ω_0 is the laser carrier frequency.

The measured ATI spectra for different IR pulse energies are shown in Figure S2. The first six peaks of the measured data points were fitted with six Gaussian functions, and the peak positions were extracted from these fits. The intensity of IR pulses was calculated using the peak positions and the equations provided above.
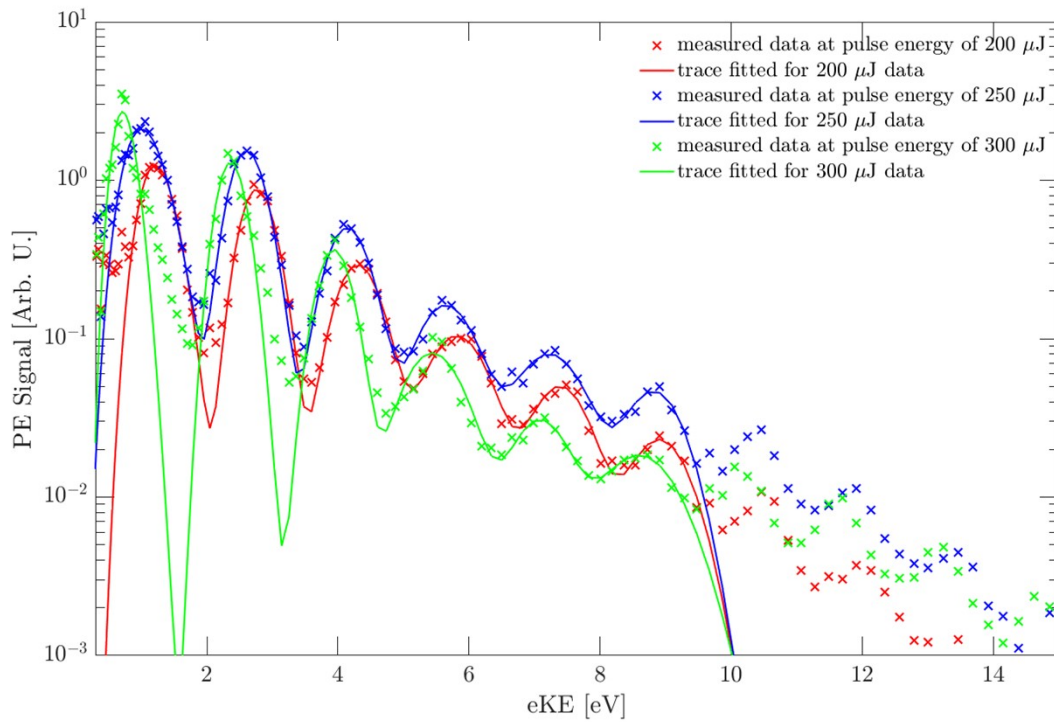
Figure S2 ATI photoelectron spectrum of Xe ionized with a focused NIR pulse with 200 μJ of energy. Intensity at focus was determined by following the shift in the ionization energy due to ponderomotive potential of the NIR field. At 200 μJ, the intensity was determined to be ~1.3x10^{13} W/cm^2 (+/- 0.2 W/cm^2).

UV intensity can also be estimated by calibrating the beam diameter with the known IR beam diameter and intensity. The estimated intensities for UV and IR pulses are presented in Table S1.

Table S1 Estimated peak intensity for BIR and UV pulses for different pulse energy/power.

NIR Pulse Energy	NIR Intensity
200 μJ	$1.3 \cdot 10^{13}$ W/cm^2
250 μJ	$1.5 \cdot 10^{13}$ W/cm^2
300 μJ	$1.9 \cdot 10^{13}$ W/cm^2

UV Pulse Power	UV Intensity
50 mW	$9.1 \cdot 10^{11}$ W/cm^2
60 mW	$1.1 \cdot 10^{12}$ W/cm^2

2. TOF spectra for different hit strengths

Figure S3 shows single-shot mass spectra of cations emitted following interaction with NIR (panel a) and UV (panel b) pulses. Figure S4 shows analogous spectra for anions. Ion mass is obtained from their corresponding TOF. Three spectra are shown in each panel, representing the strongest (yellow), medium strong (red) and weak (blue) hits. The spectra are normalized to the ion signal of Na_2Cl^+ (cations) and $NaCl_2^-$ (anions). We find that the same ion fragments are emitted for regardless of the hit strengths. In addition, relative yield for different anion fragments (Figure S4) does not depend strongly on the hit intensity.
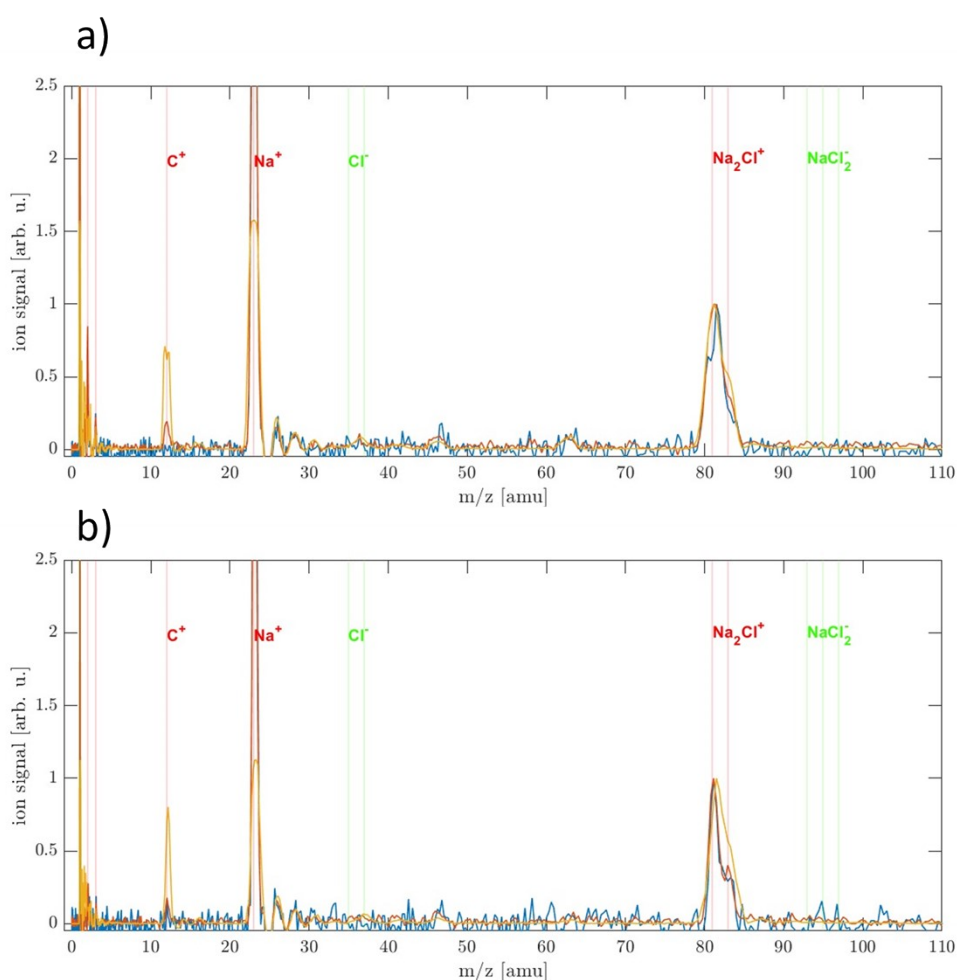
Figure S3 Representative single-shot cation TOF mass spectra for the high (yellow), medium (red) and low (blue) hit strength for NIR (panel a) and UV (panel b) pulses.
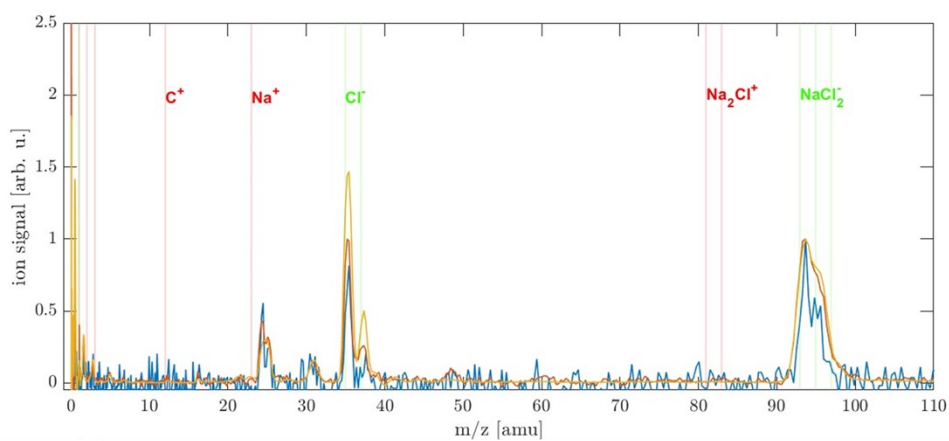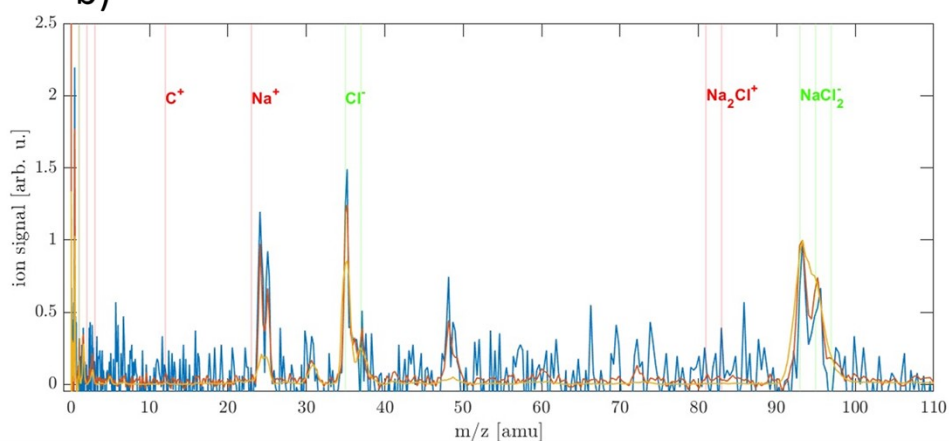
Figure S4 Representative single-shot anion TOF spectra for the high (yellow), medium (red) and low (blue) hit strength for NIR (panel a) and UV (panel b) pulses.

3. Hit rate analysis

Figure S5 show histograms of how many laser shots (expressed as hitrate, vertical axis) resulted in a specific number of illuminated pixels on the detector resulting from electron emission. For ions, Figure S6 (NIR) and Figure S7 (UV) show histograms of how many laser shots (expressed as hitrate, vertical axis) resulted in a specific number of illuminated pixels on the detector. The hitrate is higher in the NIR case as discussed in the manuscript. The histograms show similar behavior for all ions. Figure S8 shows the corresponding histograms for measurements when particles were not present in the chamber. The background results in <10 illuminated pixels for all recorded laser shots.
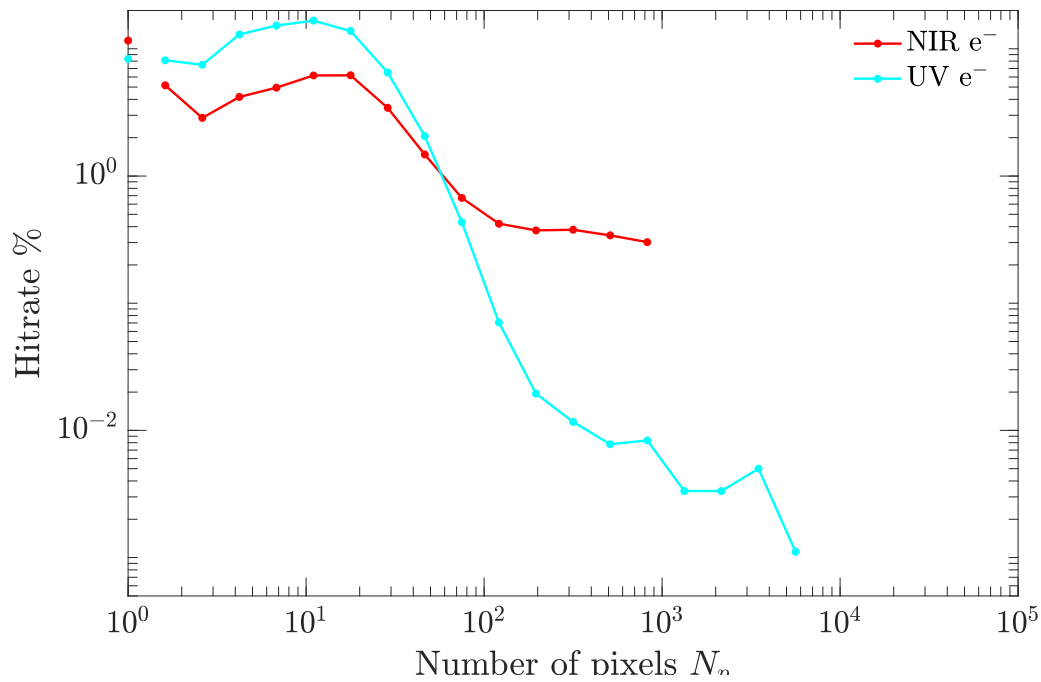
Figure S5 Hitrate (number of frames / number of laser shots) for detecting a frame with a specific number of bright pixels (N_p) for electron VMI with NIR (red line) and UV (blue line) pulses.
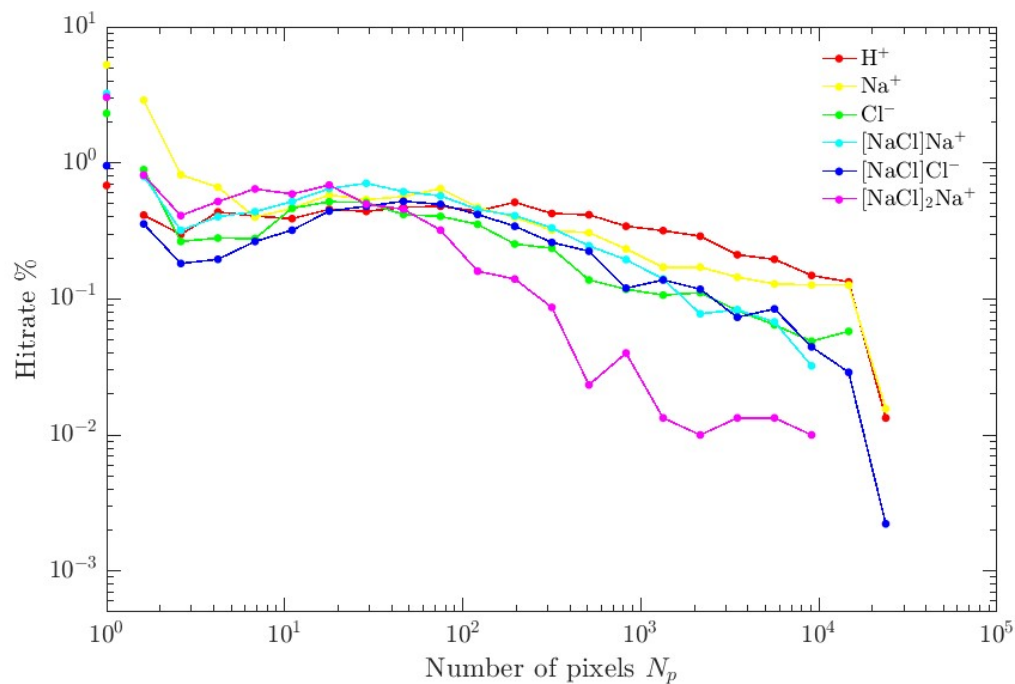
Figure S6 Hitrate (number of frames / number of laser shots) for detecting a frame with a specific number of bright pixels (N_p) for ion VMI with NIR pulses. Different ions are shown as differently colored lines, see legend.
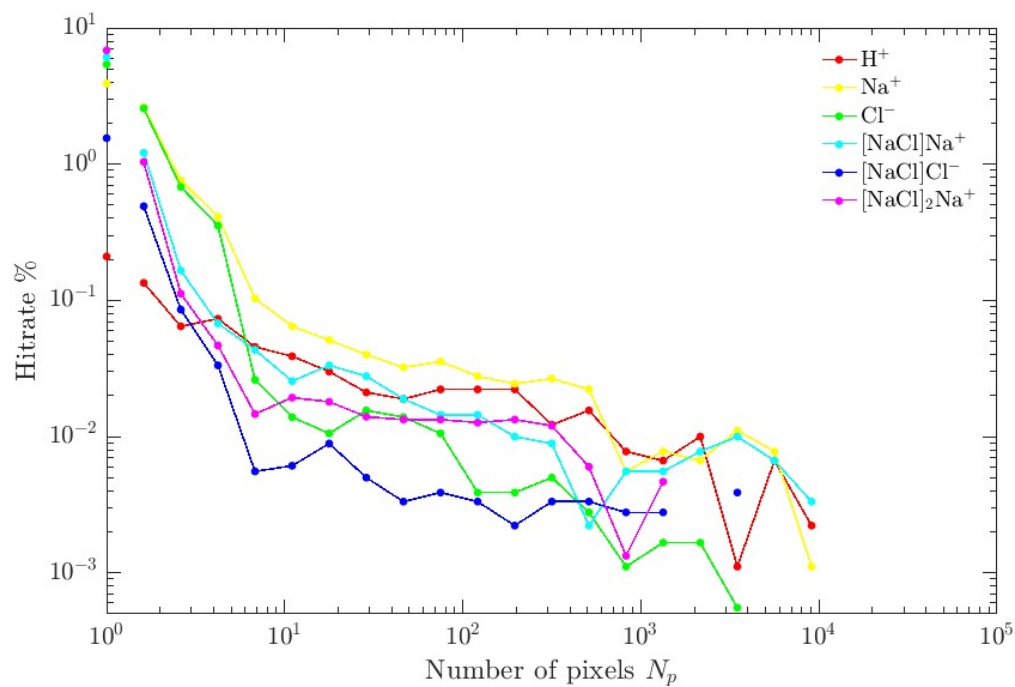
Figure S7 Hitrate (number of frames / number of laser shots) for detecting a frame with a specific number of bright pixels (N_p)for ion VMI with UV pulses. Different ions are shown as differently colored lines, see legend.
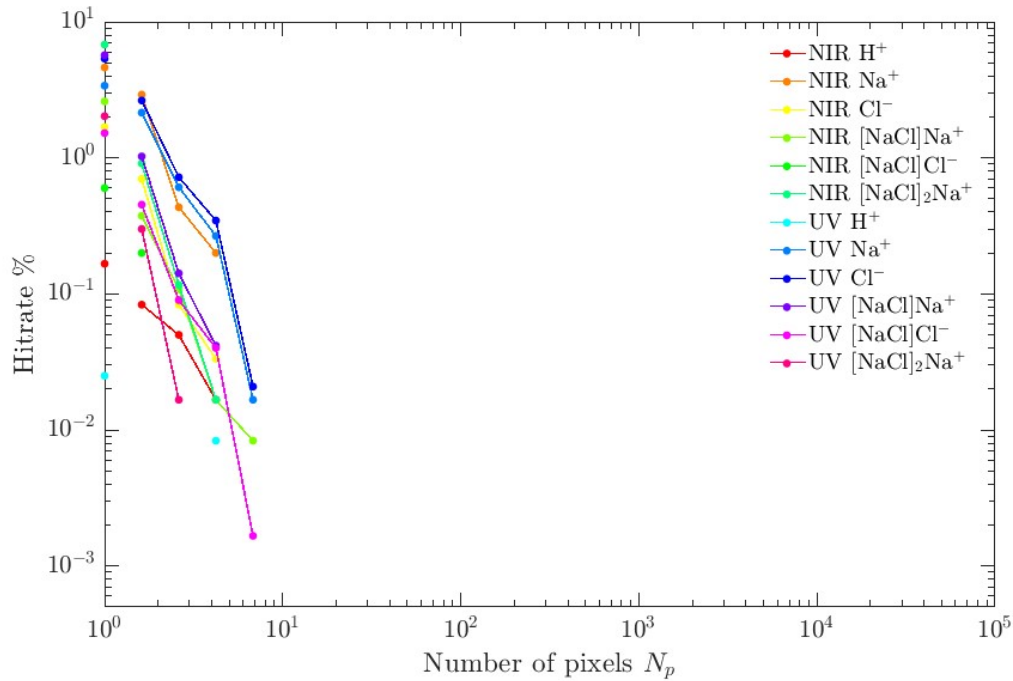
Figure S8 Hitrate (number of frames / number of laser shots) for detecting a frame with a specific number of bright pixels (N_p) for various background measurements (no particles present).

Figure S9 shows the summary of the hitrate analysis. We find ~18% (~30%) of laser shots lead to electron emission in the NIR (UV) case. Hitrates for observing ions are significantly lower, <6% (<0.4%) for NIR (UV) pulses (ions in the UV case are scaled by x20 in the figure). Hitrate also varies between different ions, with highest hitrates for H^+ and Na^+.
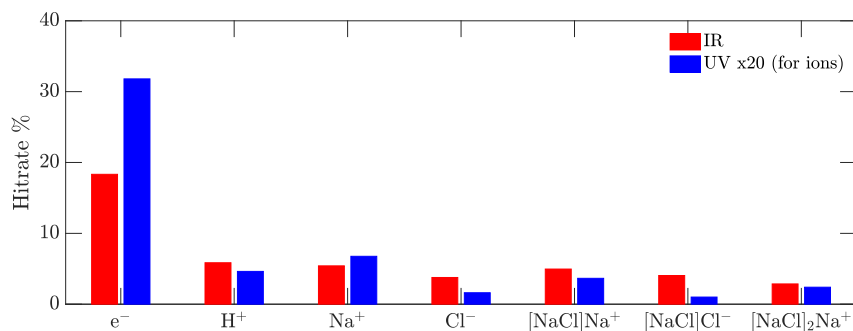
Figure S9 Hit rates determined from TOF-gated VMIs for NIR (black) and UV (red) pulses. All UV hitrates, excluding the electron peak, are scaled by a factor of 20. The inset shows a sketch of the focal plane for the NIR (left) and UV (right). Blue indicates intensities where only electron emission is expected, orange indicates regions where ions are also ejected.

4. Simulations

Figure S10 shows the visualization of the calculated 3D light intensity distributions inside NaCl particles for NIR (panels a,c,e) and UV (panels b,d,f) pulses for the three particle sizes relevant for the experiment. The light intensity is typically the highest in the central 2D slice in the plane enclosed by the laser propagation and polarization axes.
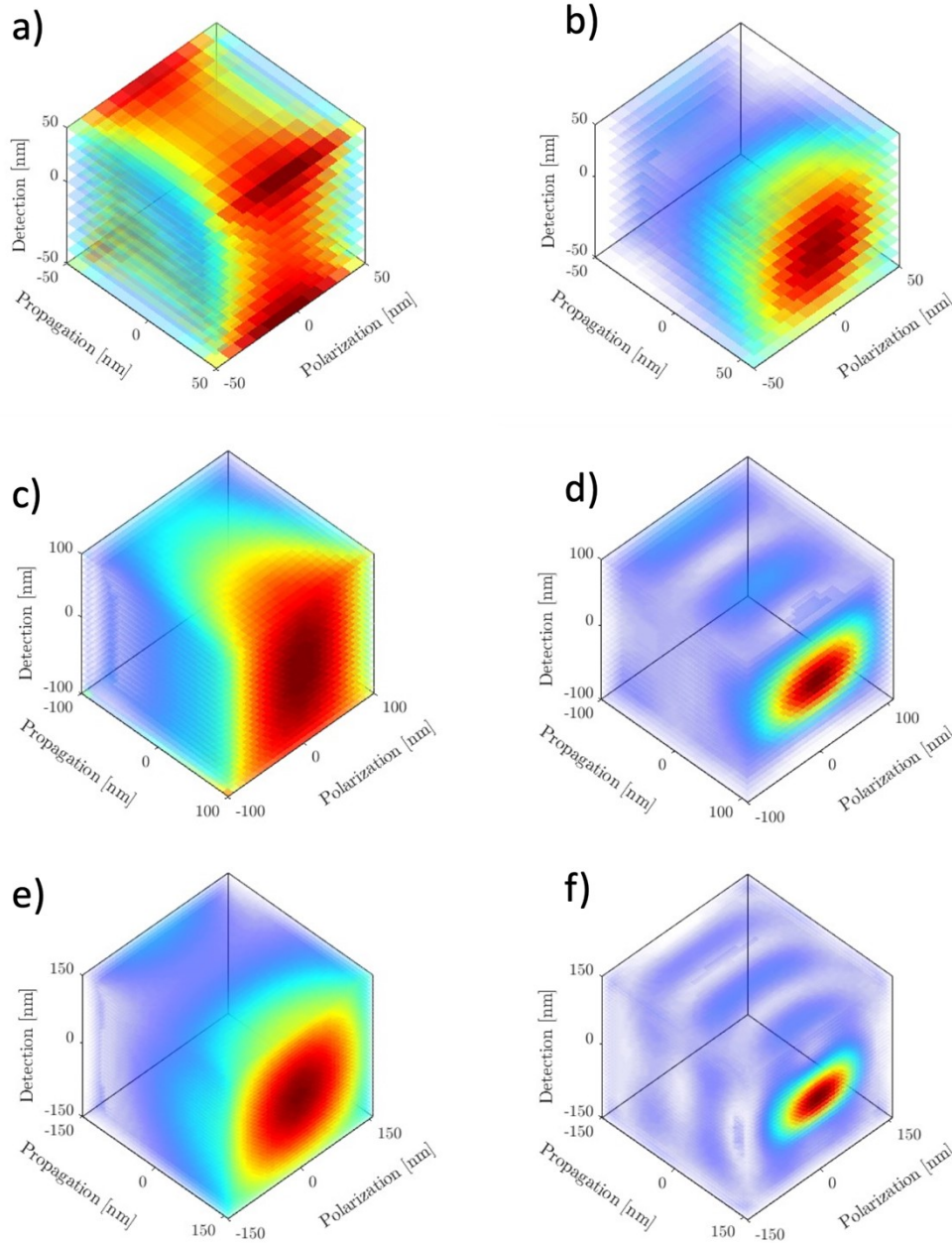
Figure S10 3D light visualization of the intensity distribution of NIR (panels a,c,e) and UV (panels b,d,f) pulses inside the NaCl particles of 100 nm (panels a-b), 200 nm (panels c-d) and 300 nm (panels e-f).

Figure S11 and Figure S12 show the time-averaged light intensity distribution obtained from FDTD calculations for NIR (panels a) and UV (panels d) pulses interacting with 200 nm (Figure S11) and 300 nm (Figure S12) particles. Time evolution of the internal intensity is then used in the rate-equations to calculate the electron density distribution. Resulting electron distributions after the laser pulse is over are shown for NIR and UV pulses in panels b and e, respectively. Time evolution of the laser intensity and total electron density at two points inside the particles is shown for NIR and UV pulses in panels c and f, respectively.
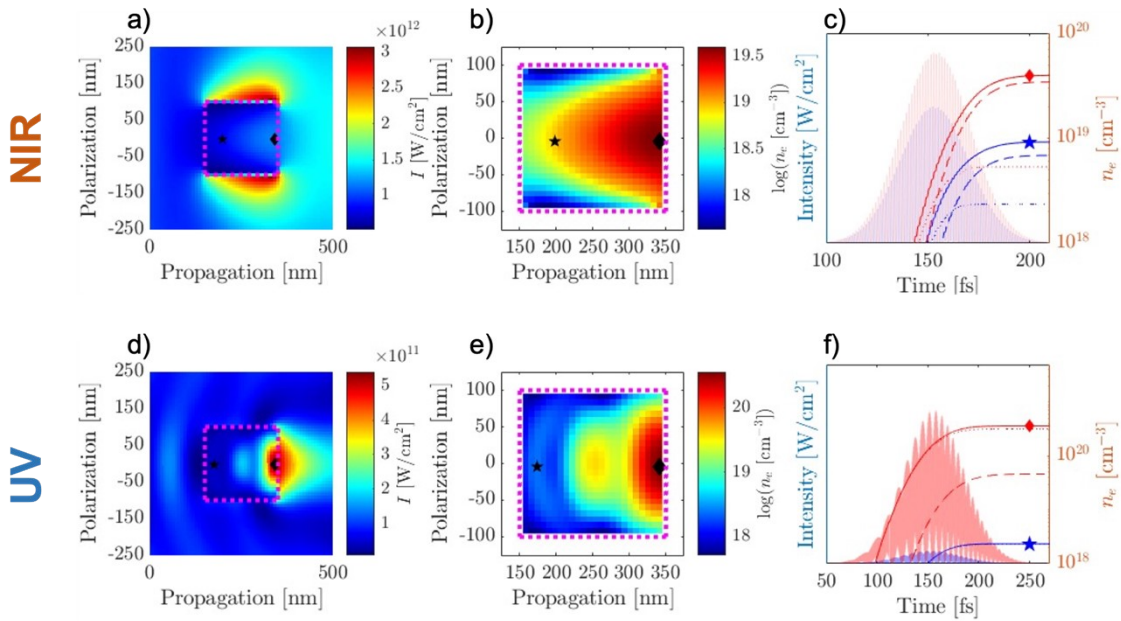
*Figure S11 **Panels a, d**: Time-averaged light intensity distributions in and around a 200nm NaCl particle for NIR (a) and UV (d) pulses. **Panels b, e**: Corresponding electron densities calculated by the rate-equation approach. **Panels c, f**: Time-evolution of the electron density at the entrance (blue, see stars in panels b,e) and exit (red, see diamonds in panels b,e) side of the particle. Total electron density is shown as full lines, photoionization contribution as dotted lines and contributions from collisional ionization as dashed lines. Time-evolution of the pulse intensity is shown as shaded blue/red curves.*
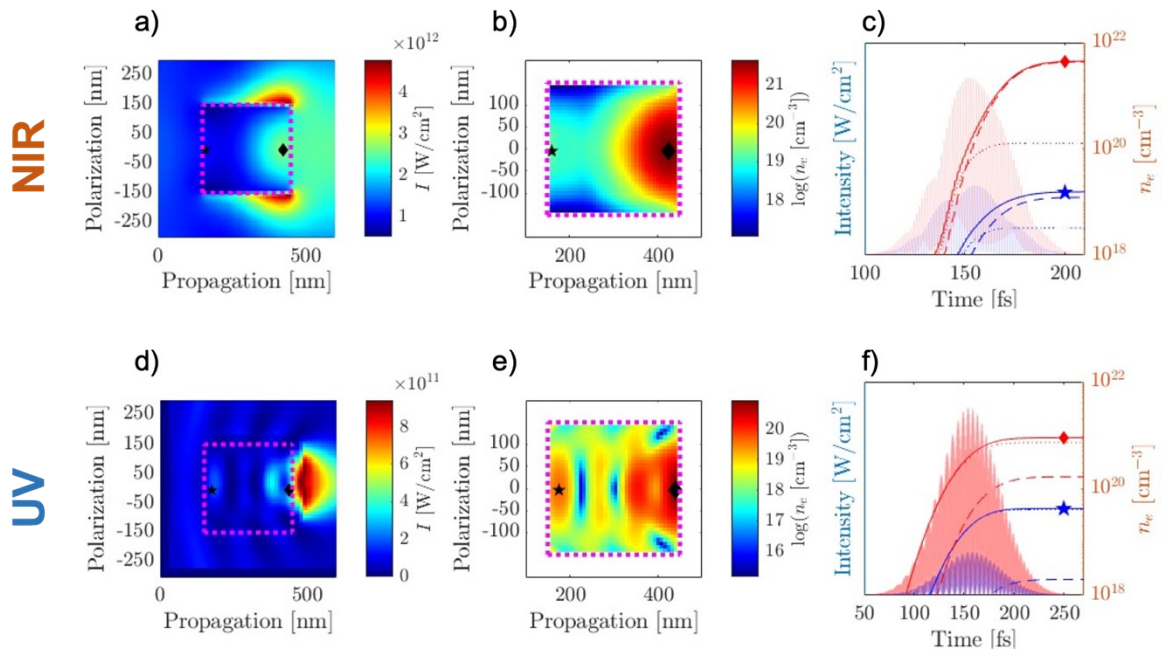
Figure S12 **Panels a, d**: *Time-averaged light intensity distributions in and around a 300nm NaCl particle for NIR (a) and UV (d) pulses.* **Panels b, e**: *Corresponding electron densities calculated by the rate-equation approach.* **Panels c, f**: *Time-evolution of the electron density at the entrance (blue, see stars in panels b,e) and exit (red, see diamonds in panels b,e) side of the particle. Total electron density is shown as full lines, photoionization contribution as dotted lines and contributions from collisional ionization as dashed lines. Time-evolution of the pulse intensity is shown as shaded blue/red curves.*

5. Time-of-flight (TOF) spectra

Cation spectra show contributions from H^+ and Na^+, as well as cluster cations $[NaCl]Na^+$ and $[NaCl]_2Na^+$. No larger clusters were observed. Protons were previously observed and attributed to fragmentation of surface-adsorbed water.[1,2] However, we note that water can also originate from NaCl in its hydrated form. Contributions from organic contaminants adsorbed on the particle surface can also be identified, e.g. C^+ (m/z=12). Such contributions were also observed previously and assigned to trace contributions from atomizer cleaning solvents,[1,2] but they could also originate from other organic contaminants within the aerosol setup. At m/z < 6 (see right panels), in addition to H^+ we observe contributions from H_2^+ and H_3^+. Such cations were recently reported in SiO_2 particles and assigned to catalytic properties of aerosolized nanoparticles in intense laser fields.[3] Our results suggest these catalytic properties could be a general phenomenon extending to other particles (NaCl) and laser fields (multi-cycle, NIR and UV).

In anion spectra, strongest contribution originates from electrons at m/z~0, while other dominant peaks can be assigned to Cl^- and $[NaCl]Cl^-$. Small contributions at m/z~50, 32 and 22 likely come from cluster anions with higher charge. At low m/z we observe a peak assigned to H^- (m/z=1) and peaks at non-integer m/z values that cannot be assigned to singly charged ion fragments. At the moment we cannot assign the origin of these peaks, but they could possibly originate from ion fragments (e.g. H^-) with rather high kinetic energy, multiply-charged fragments or delayed electron detachment from H^-/H_2^- anions. We will further investigate their origin in the upcoming work.

We note that this ion emission regime is different from studies using few-cycle femtosecond pulses where ion emission originates from photodissociation of surface adsorbates without significant ablation of the particle itself.[2,4]
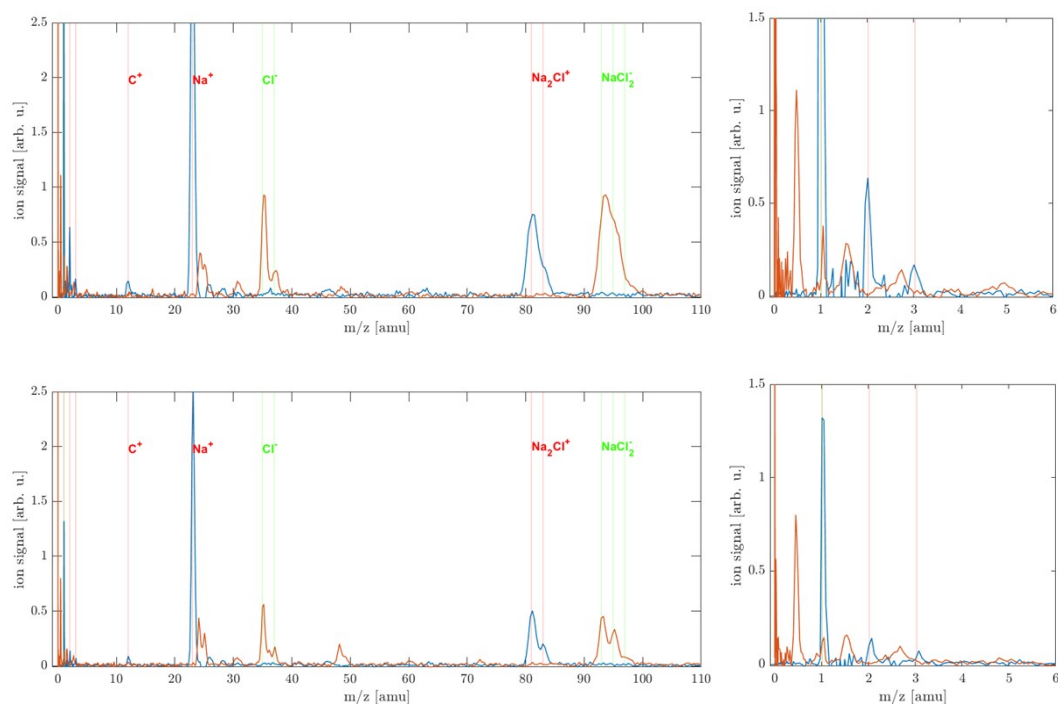
Figure S13: Ion time-of-flight spectra recorded following NIR (top panels) and UV (bottom panels) ionization of NaCl particles. Cation spectra are shown in blue and anion spectra are shown in red. Right panels show m/z region <6amu.

6. Single-shot analysis of ions

Figure S14 shows distributions of the asymmetry parameter α for various ions recorded in the case of NIR (panel a) and UV (panel b) pulses. In the NIR case, the distribution covers asymmetry parameters ranging from about -0.5 to 1, while in the UV case nearly all laser shots result in asymmetric emission with asymmetry > 0.7.
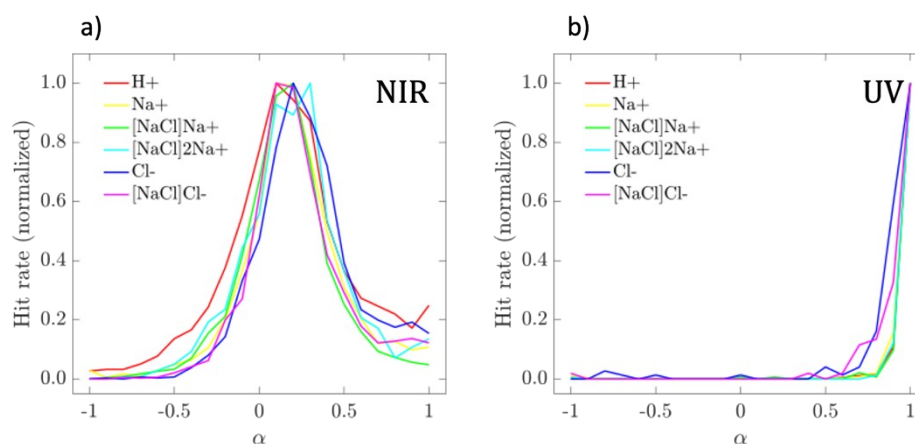
Figure S14 Distribution of forward/backward asymmetry parameter α for NIR (a) and UV (b) pulses obtained for different ions (see colors).

Figure S15 shows distributions of the average emission angle towards the light exit side of the particle for the NIR (panel a) and UV (panel b) cases. The angles span a range of $\pm 40°$ around the laser propagation axis.
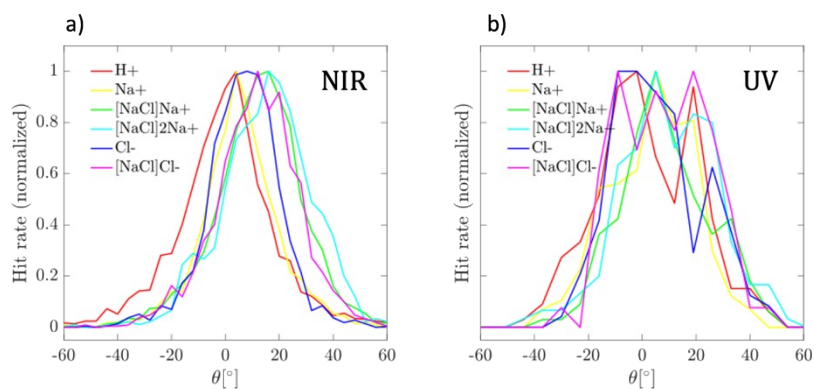
Figure S15 Hitrates for observing a frame with specific emission angle for different ions (see colors) after NIR (panel a) and UV (panel b) ionization.

Figure S16 shows distributions of the average ion kinetic energies for the NIR (panel a) and UV (panel b) cases. The results from the single-shot analysis agree well with the KE distributions reported in the main text. It is important to note that only average KE is obtained from the single-shot analysis and not the full KE distribution (as in the main text).
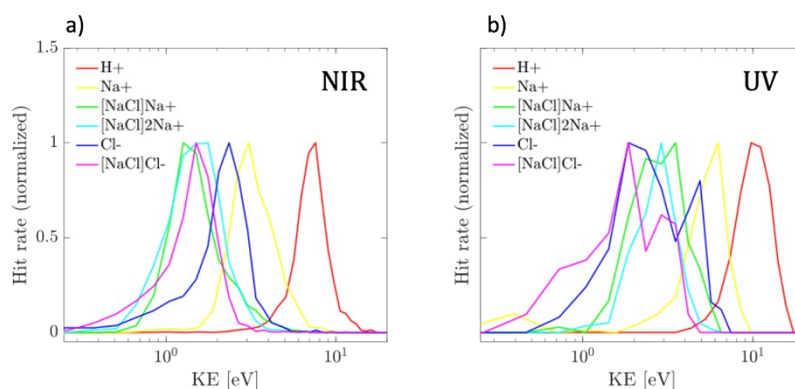
Figure S16 Hitrates for observing a frame with specific average KE for different ions (see colors) after NIR (panel a) and UV (panel b) irradiation.

Figure S17 shows the calculated light intensity distributions inside 100 nm NaCl particles for NIR/UV pulses and different particle rotation angles (columns). 3D visualizations as well as 2D slice through the center of the particle are shown. The laser propagation axis is indicated by the black line. In this visualization, the laser propagation axis is rotated by the given angle while the particle orientation remains fixed. Analogous results are shown for 200 nm (Figure S18) and 300 nm particles (Figure S19). Figure S20 shows the angular integrals corresponding to the 2D slices of the internal light intensity distribution.
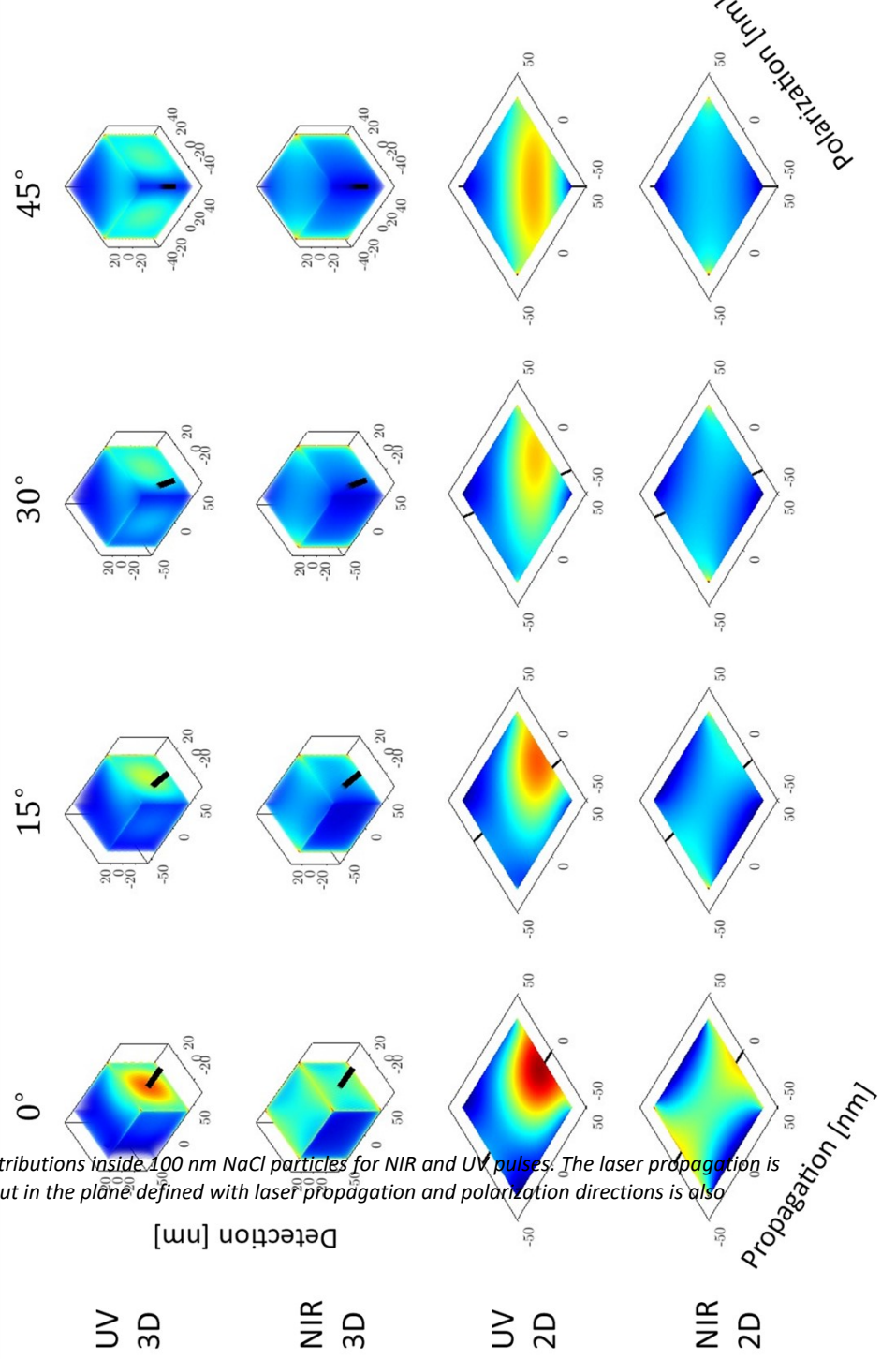
Figure S17 3D light intensity distributions inside 100 nm NaCl particles for NIR and UV pulses. The laser propagation is indicated by the black line. 2D cut in the plane defined with laser propagation and polarization directions is also shown. See labels for details.
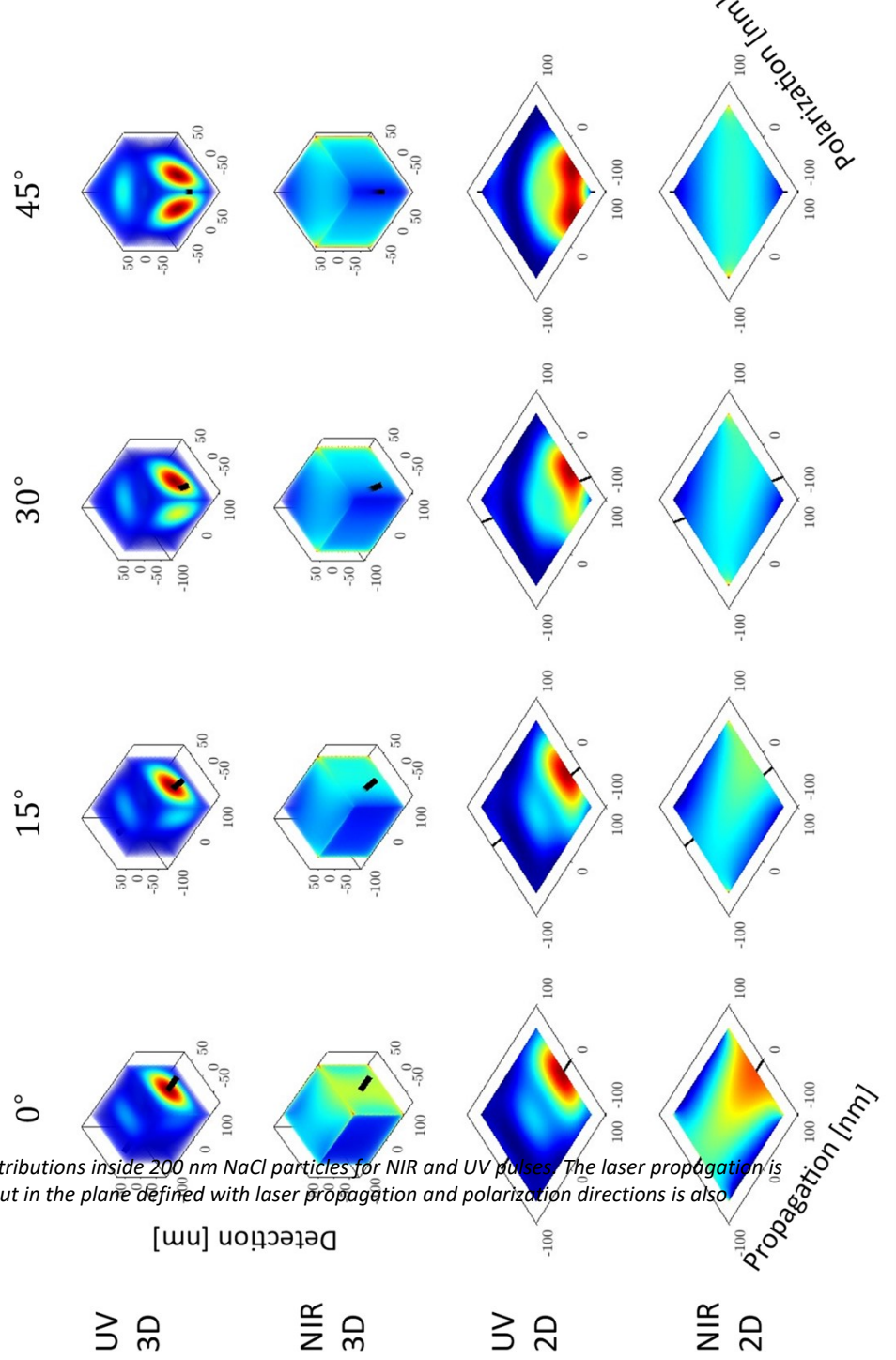
Figure S18 3D light intensity distributions inside 200 nm NaCl particles for NIR and UV pulses. The laser propagation is indicated by the black line. 2D cut in the plane defined with laser propagation and polarization directions is also shown. See labels for details.
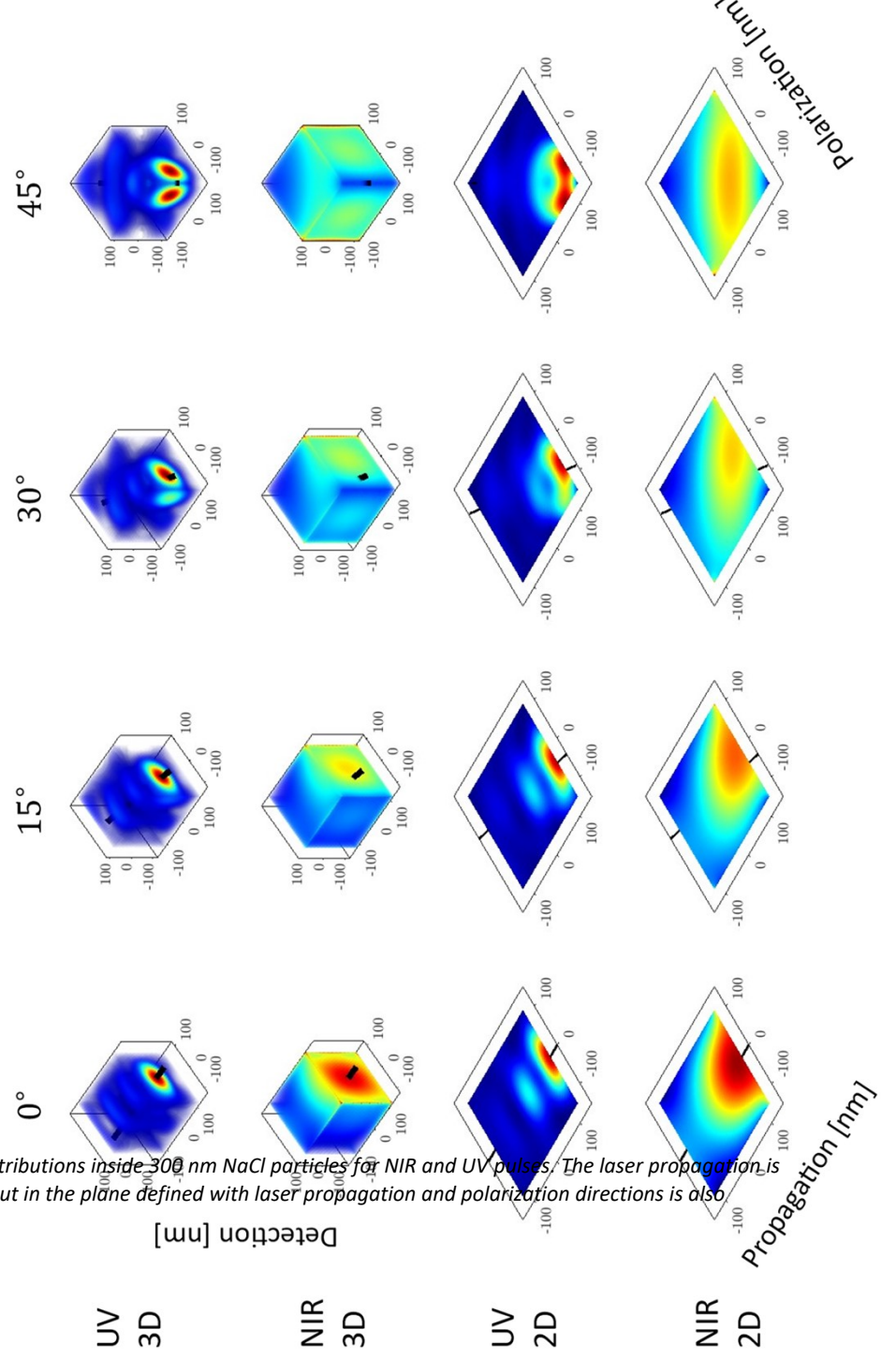
Figure S19 3D light intensity distributions inside 300 nm NaCl particles for NIR and UV pulses. The laser propagation is indicated by the black line. 2D cut in the plane defined with laser propagation and polarization directions is also shown. See labels for details.
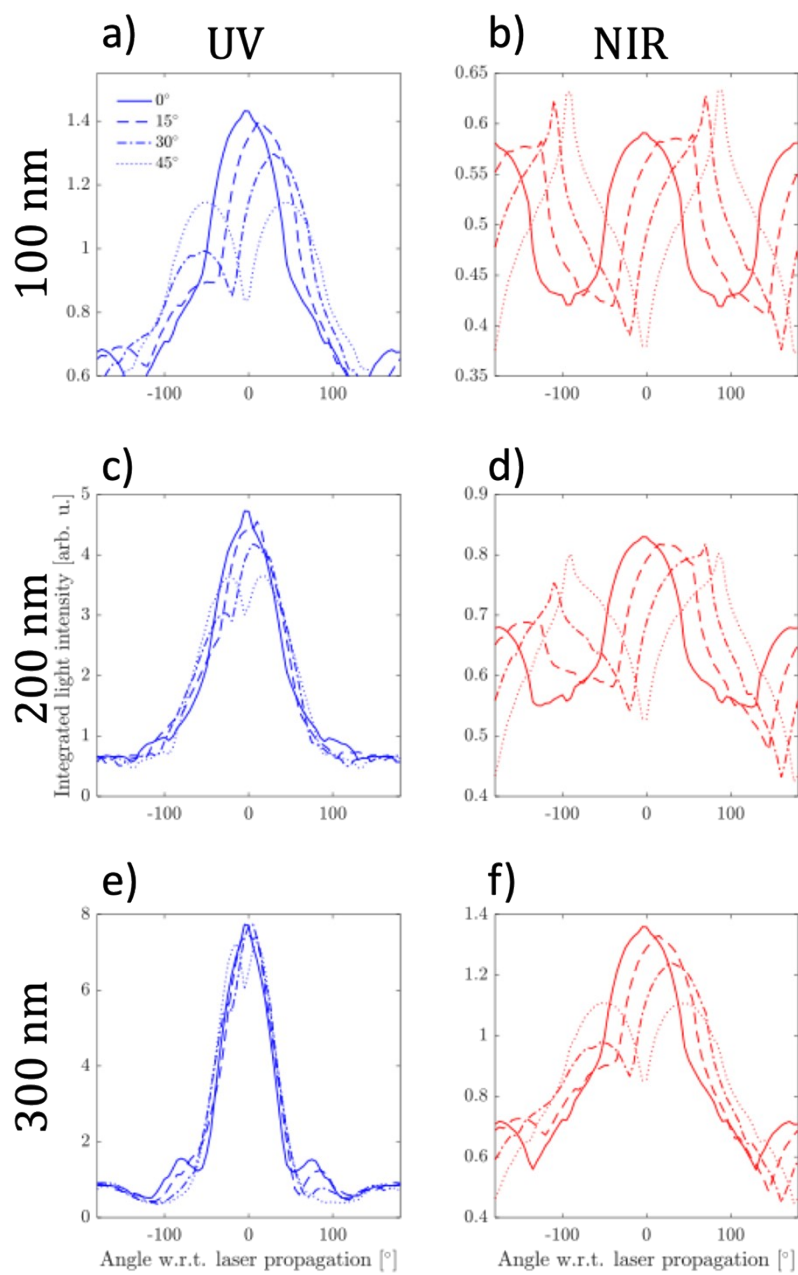
Figure S20 Angular distributions of the light intensity inside the NaCl particles for different particle orientations with respect to the laser propagation axis (see different lines). Results for UV pulses are shown in left panels and for NIR pulses in the right panels for particle sizes of 100 nm (a-b), 200 nm (c-d) and 300 nm (e-f).

Figure S21 shows the summary of the single-shot analysis for the Na$^+$ ion, analogous to the analysis for H$^+$ shown in the main text.
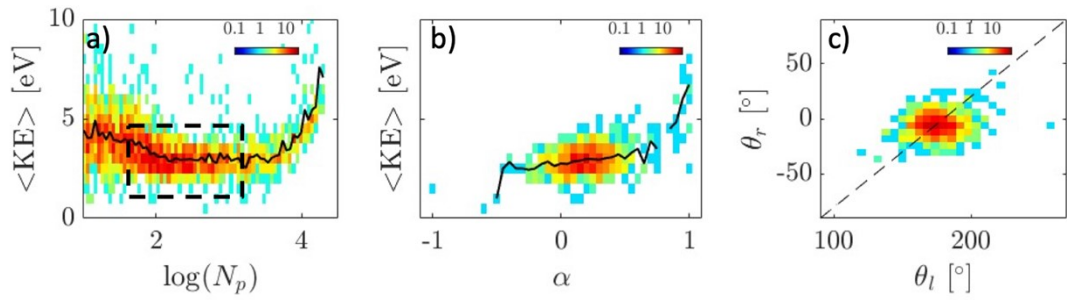
Figure S21 Single-shot analysis of Na$^+$ emission for the NIR case. Panel a: 2D histogram showing the number of frames with specific number of illuminated pixels (x-axis) and average kinetic energy (y-axis). Panel b: 2D histogram showing the number of frames with specific asymmetry (x-axis) and average kinetic energy (y-axis). Panel c: 2D histogram showing the number of frames with specific combination of emission angles.

1   D. D. Hickstein, F. Dollar, J. L. Ellis, K. J. Schnitzenbaumer, K. E. Keister, G. M. Petrov, C. Ding, B. B. Palm, J. A. Gaffney, M. E. Foord, S. B. Libby, G. Dukovic, J. L. Jimenez, H. C. Kapteyn, M. M. Murnane and W. Xiong, *ACS Nano*, 2014, **8**, 8810–8818.

2   P. Rupp, C. Burger, N. G. Kling, M. Kübel, S. Mitra, P. Rosenberger, T. Weatherby, N. Saito, J. Itatani, A. S. Alnaser, M. B. Raschke, E. Rühl, A. Schlander, M. Gallei, L. Seiffert, T. Fennel, B. Bergues and M. F. Kling, *Nat. Commun.*, 2019, **10**, 1–7.

3   M. S. Alghabra, R. Ali, V. Kim, M. Iqbal, P. Rosenberger, S. Mitra, R. Dagar, P. Rupp, B. Bergues, D. Mathur, M. F. Kling and A. S. Alnaser, *Nat. Commun.*, 2021, **12**, 3839.

4   P. Rosenberger, P. Rupp, R. Ali, M. S. Alghabra, S. Sun, S. Mitra, S. A. Khan, R. Dagar, V. Kim, M. Iqbal, J. Schötz, Q. Liu, S. K. Sundaram, J. Kredel, M. Gallei, C. Costa-Vera, B. Bergues, A. S. Alnaser and M. F. Kling, *ACS Photonics*, 2020, **7**, 1885–1892.